Article

Highly Selective Artificial K⁺ Transporters Reverse Liver Fibrosis In Vivo

Qiuping Zhang, Qinghong Liang, Guijiang Wang, Xiaopan Xie, Yin Cao, Nan Sheng, Zhiping Zeng, and Changliang Ren*

Cite This: JACS Au 2024, 4, 3869−3883

Read Online

ACCESS | Metrics & More | Article Recommendations | SI Supporting Information

ABSTRACT: Liver fibrosis is a life-threatening disease that currently lacks clinically effective therapeutic agents. Given the close correlation between dysregulated intracellular K⁺ homeostasis and the progression of liver fibrosis, developing artificial K⁺ transporters mimicking the essential function of their natural counterparts in regulating intracellular K⁺ levels might offer an appealing yet unexplored treatment strategy. Here, we present an unconventional class of artificial K⁺ transporters involving the "motional" collaboration between two K⁺ transporter molecules. In particular, **6C6** exhibits an impressive EC_{50} value of 0.28 μM (i.e., 0.28 mol % relative to lipid) toward K⁺ and an exceptionally high K⁺/Na⁺ selectivity of 15.5, representing one of the most selective artificial K⁺ transporters reported to date. Most importantly, our study demonstrates, for the first time, the potential therapeutic effect of K⁺-selective artificial ion transporters in reversing liver fibrosis both *in vitro* and *in vivo*.
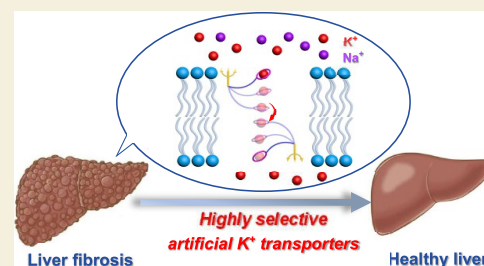
KEYWORDS: *artificial potassium transporters, transmembrane K⁺ transport, membrane-active molecular machines, liver fibrosis*

INTRODUCTION

Potassium ion channels are integral membrane proteins that play crucial roles in maintaining cellular function by regulating the flow of K⁺ ions across the cell membranes. They are fundamental for numerous physiological processes, including the regulation of cell excitability, muscle contraction, and hormonal secretion.[1] Dysregulation of K⁺ transport can lead to various life-threatening diseases, such as live fibrosis, pulmonary arterial hypertension, and cancer.[2−5] Over the past four decades, considerable efforts have been made toward the development of artificial K⁺ transporters as structurally simpler models of the natural counterparts to potentially address diseases arising from K⁺ ion transport dysregulation.[6] This strategy requires the highly active and selective transport of K⁺ ions, mediated by artificial transporters. Nevertheless, in contrast to the natural K⁺ channels, such as the KcsA channel, which exhibits exceptionally high K⁺/Na⁺ selectivity of 1,000,[7] strategies to construct artificial K⁺ transporters with K⁺/Na⁺ selectivity greater than 10 remain limited. Current efforts in this direction have mainly focused on one-dimensionally assembled crown ethers[8−11] or self-assembled/unimolecular organic nanotubes with confined cavities.[12−15] Moreover, the potential application of K⁺-selective transporters in addressing diseases associated with dysregulation of intracellular K⁺ homeostasis remains unexplored.

Liver fibrosis is an abnormal wound-healing process that occurs in response to a variety of chronic liver injuries, including alcohol abuse, drug toxicity, viral infections, nonalcoholic fatty liver disease (NAFLD), and so on.[16−20]

The pathology of liver fibrosis is characterized by the excessive accumulation of extracellular matrix (ECM), which culminates in the formation of fibrous tissue disrupting the normal physiological function of the liver. Failure to address persistent liver fibrosis can result in liver cirrhosis, liver failure, and even liver cancer.[21−24] At present, however, there is no clinically effective drug for treating liver fibrosis.[25,26]

Extensive studies have established that activation and abnormal proliferation of hepatic stellate cells (HSCs) play a pivotal role in the progression of liver fibrosis by producing ECM.[19,20,27] Injured hepatocytes secrete cytokines to activate the quiescent HSCs.[28] The autocrine cytokines released by activated HSCs then perpetuate this activation loop. There is growing evidence indicating that transforming growth factor-β 1 (TGF-β1) is one of the most critical cytokines that mediate the progression of liver fibrosis.[29,30] Upon binding with its receptor (TGFβR2) on the cell membrane, it triggers the downstream TGF-β/Smad signaling pathway to activate HSCs (Figure 1a).[31] Accordingly, targeting TGF-β/Smad signaling pathway has emerged as a promising strategy for combating liver fibrosis.[32−34] Recent reports have elucidated that dysregulated intracellular K⁺ homeostasis, arising from the
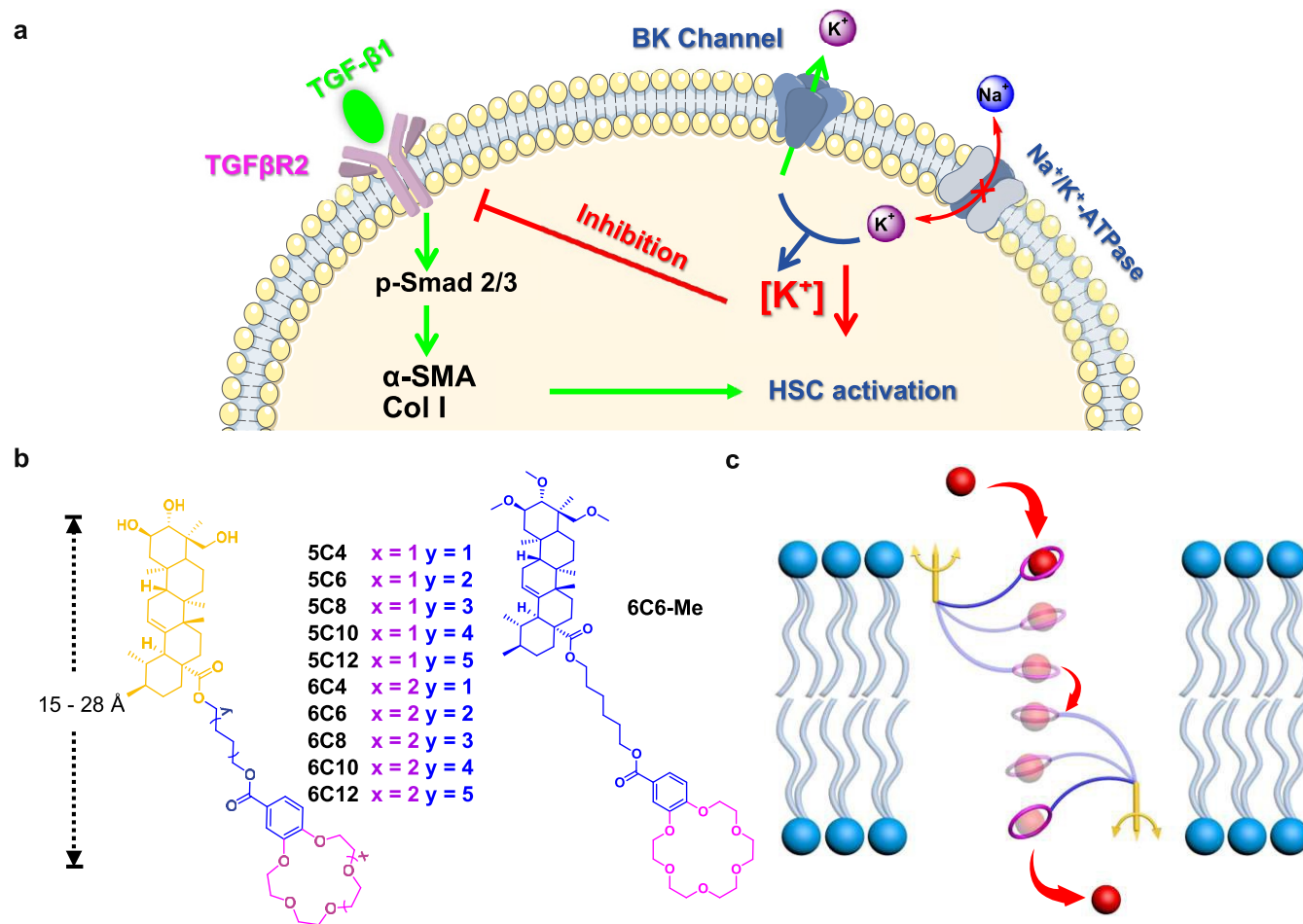
Figure 1. Molecular design and proposed K^+ transport mechanisms. (a) Attenuation of intracellular K^+ level through the activation of Big Potassium (BK) channels or inhibition of Na^+/K^+-ATPase results in the downregulation of the expression of TGFβR2 and the subsequent inhibition of the activation of HSCs through impeding the TGF-β/Smad signaling pathway. TGFβR2 = transforming growth factor-β receptor 2. HSC = hepatic stellate cell. The Figure was partly generated using Servier Medical Art, provided by Servier, licensed under a Creative Commons Attribution 3.0 unported license. (b) Molecular design of the ion transporters. (c) Schematic illustration for the transmembrane transport of K^+ ions involving the motional collaboration of two transporter molecules.

malfunction of natural K^+ transporters, such as Na^+/K^+-ATPase and Big Potassium (BK) channel, can have a significant impact on the expression of TGFβR2.[2,3,35−38] Therefore, we hypothesize that developing highly actively and selective artificial K^+ transporters capable of efficiently regulating the intracellular K^+ levels might offer an appealing strategy for the treatment of liver fibrosis.

Here, we describe an unconventional class of artificial K^+ transporters involving the "motional" collaboration between two K^+ transporter molecules, with one positioned at the top and the other at the bottom side of the membrane. The molecular design strategy involves utilizing asiatic acid (**AA**) as the lipid anchor, with crown ethers serving as the cation-binding units that connect to the lipid anchor through hydrophobic alkyl chains. Through combinatorial tailoring of the length of the alkyl chains and the type of crown ethers, we successfully identified an exceptionally active and selective K^+ transporter, **6C6**. **6C6** facilitates the transport of K^+ ions across the membrane with an impressive EC_{50} value of 0.28 μM (i.e., 0.28 mol % relative to lipid) and a remarkable K^+/Na^+ selectivity ratio of 15.5, which is among the top-notch K^+-selective transporters to date. For the first time, **6C6** exhibits both a prominent antiproliferative effect on TGF-β1-activated

HSCs and a significant inhibitory effect on HSC activation. These effects can be attributed to the highly active and selective efflux of intracellular K^+ ions mediated by **6C6**. This, in turn, induces cell apoptosis, arrests cell cycle progression, and inhibits HSC activation through the downregulation of TGFβR2 expression, which effectively impedes the TGF-β/Smad signaling pathway. Excitingly, employing the CCl$_4$-induced liver fibrosis rat model, the *in vivo* efficacy of **6C6** in ameliorating liver fibrosis was successfully demonstrated with minimal toxicity.

■ RESULTS AND DISCUSSION

Molecular Design

Recently, membrane-active molecular machines have emerged as a novel class of ion transporters, providing alternative ion transport means that bypass the conventional channel and carrier mechanisms.[39,40] Early elegant examples included molecular motors,[41−43] molecular shuttles,[44] molecular ion fishers,[45] molecular dodecapuses,[46] molecular swings,[47] and so on.

Drawing inspiration from this concept, in the present study, we designed ion transporters **mCn** (m = 5, 6; n = 4−12) by appending cation-binding crown ethers to asiatic acid via
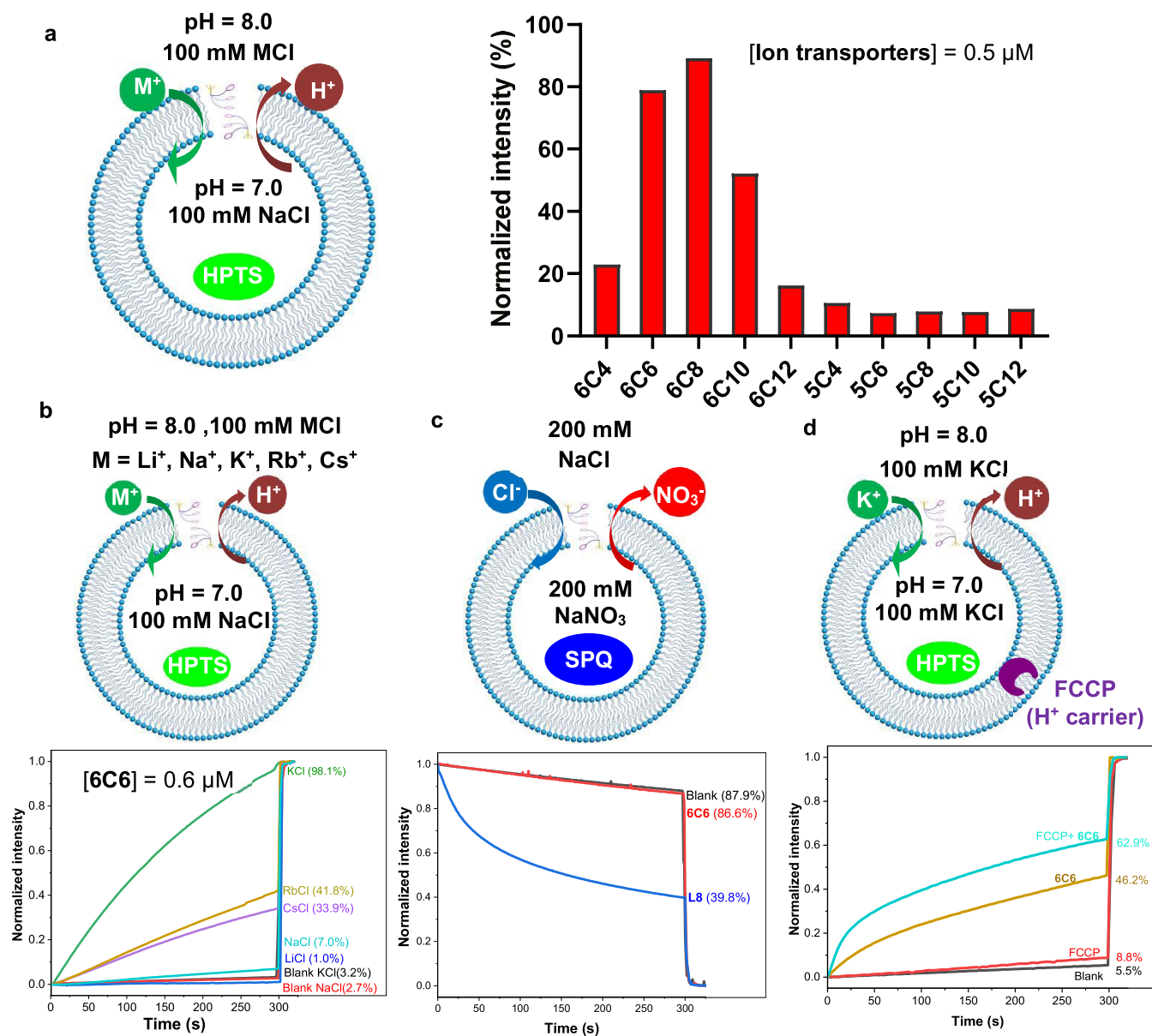
Figure 2. Transmembrane ion transport activity, selectivity, and mechanism study of ion transporters. (a) K$^+$ ion transport percentages (R$_{K^+}$) for various transporters at 0.5 μM. (b) Alkali metal ion transport curves for **6C6** are shown at 0.6 μM. (c) SPQ assay to confirm the inability of **6C6** to transport Cl$^-$ ions, [**6C6**] = 1.0 μM, [**L8**] = 10.0 μM. SPQ = 6-methoxy-N-(3-sulfopropyl) quinolone. (d) FCCP-based HPTS assay confirms that **6C6** demonstrates a preferred ion transport for K$^+$ over H$^+$ ions, [**6C6**] = 0.4 μM, [FCCP] = 5.0 nM, FCCP = carbonyl cyanide 4-(trifluoromethoxy) phenylhydrazone, HPTS = 8-hydroxypyrene-1,3,6-trisulfonic acid.

flexible alkyl chains of varying length, as shown in Figure 1b. Asiatic acid possesses three hydroxy groups at its end serving as lipid anchors and a chiral rigid pentacyclic triterpenoid scaffold that could control the motion of crown ethers due to its steric hindrance. In total, ten ion transporters were modularly synthesized using two types of crown ethers (18-crown-6 and 15-crown-5) and five types of alkyl linkers (n-C$_4$H$_8$, n-C$_6$H$_{12}$, n-C$_8$H$_{16}$, n-C$_{10}$H$_{20}$, and n-C$_{12}$H$_{24}$). Of particular interest is **6C6**, which contains an 18-crown-6 unit and an n-C$_6$H$_{12}$ alkyl linker. The computationally optimized structure in the membrane reveals that its cation-binding crown ether unit is located near the center region of the membrane (Figure S11a). We therefore reasoned that **6C6** might mediate the transport of ions across the membrane involving the collaboration of two **6C6** molecules, with one positioned at the top and the other at the bottom side of the membrane (Figure 1c). In our proposed

ion transport process, the crown ether of **6C6** anchored at one side of the membrane captures an ion and undergoes a swinging motion to transport the captured ion across the hydrophobic region of the membrane, driven by the ionic concentration gradient. When two crown ether units of **6C6** anchoring at the opposite side of the membrane meet head-to-head at the central membrane region, where the cation experiences the highest energetic penalty, an ion-relay process takes place. Subsequently, the second **6C6** swoops the ion to the other side of the membrane to complete the trans-membrane process with relatively defined ion transport pathways, showing single-channel behavior.

Ion Transport Activity and Selectivity

The ability of designed ion transporters to mediate K$^+$ across the lipid membrane was initially evaluated using a well-

established 8-hydroxypyrene-1,3,6-trisulfonic acid (HPTS) assay (Figure 2a). In this assay, large unilamellar vesicles (LUVs) encapsulating pH-sensitive HPTS dye (1.0 mM) and NaCl (100 mM) in 4-(2-hydroxyethyl)-1-piperazineethanesulfonic acid (HEPES) buffer at pH = 7.0 were prepared from egg yolk phosphatidylcholine (EYPC). Subsequently, these LUVs were exposed to a HEPES buffer containing KCl (100 mM) at pH = 8.0, thereby establishing a transmembrane pH gradient (ΔpH) of 1.0. After incorporating ion transporters at a final concentration of 0.5 μM (i.e., 0.5 mol % relative to lipid), the increments in the ratiometric value of HPTS fluorescence at 510 nm (I_{460}/I_{403}) were recorded for a period of 300 s. At 300 s, LUVs were disintegrated upon incorporation of Triton X-100, and the resulting ratiometric value of the HPTS fluorescence at 510 nm (I_{460}/I_{403}) was normalized to 100%.

As illustrated in Figure 2a, the results obtained from the HPTS assay demonstrated that ion transporters containing 18-crown-6 exhibited significantly higher K$^+$ transport activity compared to those containing 15-crown-5. Among the ten compounds tested, 6C8, which consists of 18-crown-6 and n-C$_8$H$_{16}$ alkyl linker, exhibited the highest fractional K$^+$ transport activity of 89% at a concentration of 0.5 μM. Apparently, the length of the alkyl linker also exerted a remarkable influence on the ion transport activities. Upon increasing the length of the alkyl linkers from n-C$_4$H$_8$ to n-C$_8$H$_{16}$, a consistent increase in K$^+$ transport activities was observed. However, further elongation of the alkyl linker resulted in a significant decrease in K$^+$ transport activity. Inferred from the combined hydrophobic length of the fully extended 6C10 and 6C12 reaches 25 and 28 Å, respectively, these ion transporters may transport K$^+$ across the membrane through a unimolecular mechanism, which is energetically less favorable.

As K$^+$ and Na$^+$ ions are the most physiologically relevant alkali metal ions, particularly in correlation to the expression of TGFβR2, the EC$_{50}$ values of the ion transporters involved in mediating the transport of K$^+$ and Na$^+$ were determined using Hill analysis (Figure S1). The reciprocal ratio of the EC$_{50}$ values can be potentially used to quantify the ion transport selectivity between K$^+$ and Na$^+$. As summarized in Table 1,

Table 1. Determined Values for EC$_{50}$ (μM), EC$_{50}$ (Na$^+$)/EC$_{50}$ (K$^+$), and R$_{K^+}$/R$_{Na^+}$

	EC$_{50}$ for K$^+$ (μM)	EC$_{50}$ for Na$^+$ (μM)	EC$_{50}$(Na$^+$)/EC$_{50}$(K$^+$)	R$_{K^+}$/R$_{Na^+}$
6C4	0.68 ± 0.02	13.0 ± 1.3	19.1	9.1
6C6	0.28 ± 0.02	13.6 ± 1.5	48.7	22.3
6C8	0.25 ± 0.02	3.8 ± 0.3	15.2	8.7
6C10	0.72 ± 0.03	>100	>138	11.7
6C12	3.2 ± 0.1	>100	>31	16.7
5C4	17.2 ± 0.3	5.0 ± 0.5	0.29	0.14
5C6	18.2 ± 1.1	2.5 ± 0.1	0.14	0.25
5C8	43.4 ± 7.4	24.5 ± 4.2	0.55	0.73
5C10	>100	>100	N. D.	N. D.
5C12	>100	>100	N. D.	N. D.

6Cns generally demonstrated both good activity and selectivity toward K$^+$. Specifically, the EC$_{50}$ values for K$^+$ were determined to range from 0.25 to 3.2 μM, corresponding to 0.25 to 3.2 mol % relative to lipid. Furthermore, the reciprocal ratios of the EC$_{50}$ values between K$^+$ and Na$^+$ were calculated to range from 15.2 to >138. However, it should be noted that at high concentrations, the ion transporters may have poor

solubility or undergo self-aggregation. As a consequence, the reciprocal ratios of the corresponding EC$_{50}$ values may not accurately represent the actual ion selectivity. Alternatively, we used fractional fluorescence intensity ratios (R$_{K^+}$/R$_{Na^+}$), which is another widely adopted and reliable index for assessing ion transport selectivity.[14,45,46,48] In this approach, we obtained the normalized fractional fluorescence intensity (R$_{M^+}$) at a specific concentration of the transporter where the transport activity for the most active ion exceeds 90% for a period of 300 s. Employing this index, all of the 6Cns were still observed to exhibit excellent selectivity toward K$^+$, as evidenced by the remarkable R$_{K^+}$/R$_{Na^+}$ ratio ranging from 8.7 to 22.3 (Table 1), highlighting the exceptional selectivity of the 6Cns toward K$^+$ over Na$^+$.

A comprehensive analysis of the ion transport activity and selectivity revealed that the elongation of the alkyl linker from n-C$_4$H$_8$ to n-C$_6$H$_{12}$ resulted in a substantial enhancement of both the K$^+$ transport activity and selectivity. Upon elongation of the alkyl linker to n-C$_8$H$_{16}$, a slight improvement in the K$^+$ transport activity was observed. However, this was accompanied by a significant decrease in K$^+$/Na$^+$ selectivity from 22.3 to 8.7. Further elongation of the alkyl linker to n-C$_{12}$H$_{24}$ revealed a notable trend characterized by a gradual decrease in K$^+$ transport activity coupled with a gradual increase in K$^+$/Na$^+$ selectivity, indicating that ion transport mechanisms involving short alkyl linkers may differ from those with longer alkyl linkers. Among the five 6Cn ion transporters, 6C6, characterized by its length that matches half the width of the membrane, exhibited both excellent activity (EC$_{50}$ = 0.28 μM) and selectivity (R$_{K^+}$/R$_{Na^+}$ = 22.3) for K$^+$, which is clearly among the top-notch K$^+$-selective transporters reported over the past four decades.

The ion selectivity of 6C6 for alkali metal ions followed the trend K$^+$ > Rb$^+$ > Cs$^+$ > Na$^+$ > Li$^+$, in accordance with Eisenman sequence IV (Figure 2b),[49] indicating that the selectivity is dominated by the specific recognition of ions by crown ether units rather than ionic radius or ion dehydration energy. In contrast, except for 5C10 and 5C12, which exhibited poor ion transport activity for both K$^+$ and Na$^+$ ions, 5C4, 5C6, and 5C8 from 5Cns ion transporters demonstrated a notable preference for transporting Na$^+$ over K$^+$, with 5C4 being the most selective Na$^+$ transporter (R$_{Na^+}$/R$_{K^+}$ = 7.1). This result implied that the ion transport selectivity of transporter relays was also dependent on the type of crown ether units. In general, the ion transport efficiency of K$^+$-selective transporters 6Cns was observed to be more than 1 order of magnitude higher than that of the Na$^+$-selective transporters 5Cns, probably due to the lower dehydration energy associated with K$^+$ ions.

Given the excellent activity and selectivity of 6C6 toward K$^+$, it was selected for further ion transport mechanism study. The possibility of 6C6 facilitating the transmembrane transport of chloride was ruled out by a chlorine-sensitive 6-methoxy-N-(3-sulfopropyl) quinoline (SPQ) assay. In sharp contrast to the reported chloride channel L8,[50] which induces 54.7% of fluorescence quenching of SPQ at 10.0 μM, 6C6 causes negligible fluorescence quenching of SPQ even at 1.0 μM (Figure 2c). Additionally, Figure S3 shows that varying the extravesicular buffer from KCl to KI in the HPTS assay results in negligible changes in the ion transport activities after background correction. In combination with the results obtained from the SPQ assay, our findings suggest minimal
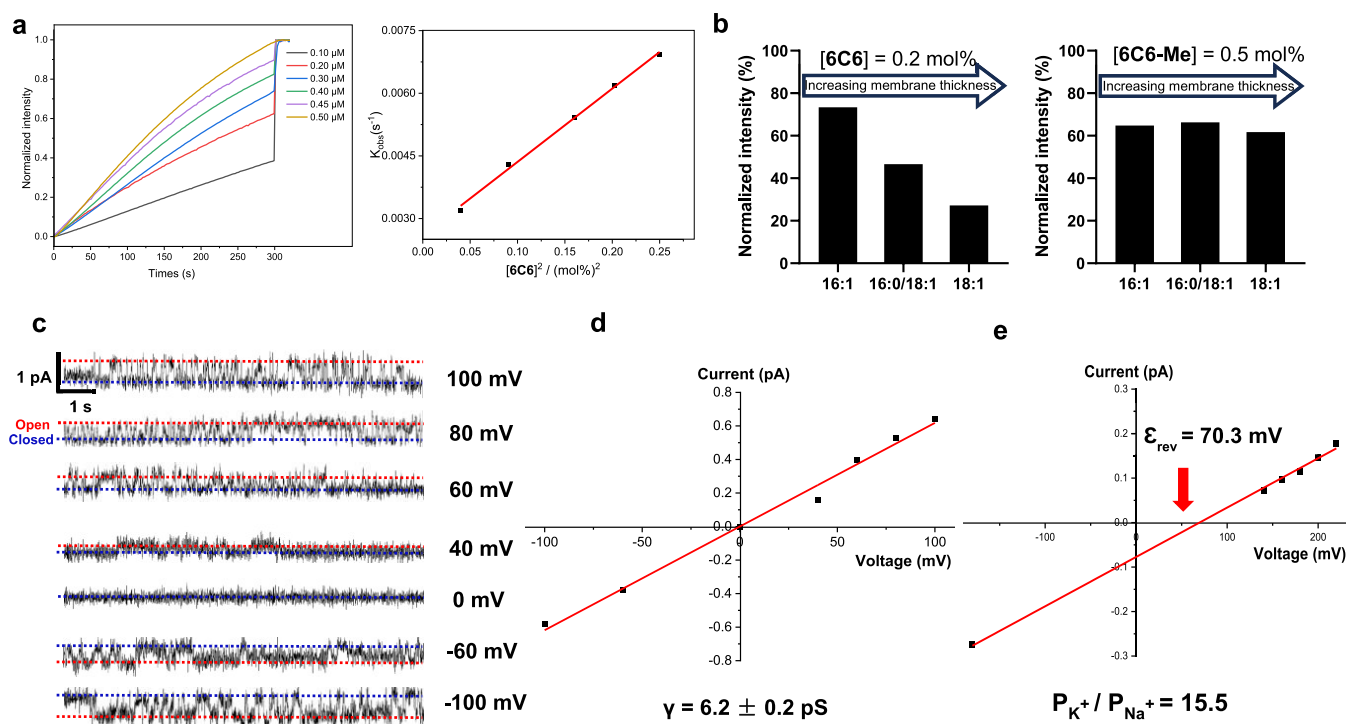
Figure 3. Transmembrane ion transport mechanism study of **6C6**. (a) Concentration dependence of relay's K$^+$ transport activity with preincorporated **6C6** and linear relationship for the K$^+$ influx rate constants (K_{obs}) with $[\mathbf{6C6}]^2$. (b) K$^+$ transport activity of **6C6** (0.2 mol %) and **6C6-Me** (0.5 mol %) in the LUVs with varying membrane thickness. (c) Single-channel current traces and (d) current−voltage (I−V) curve for **6C6** were recorded in symmetric baths (*cis* chamber = *trans* chamber = 1.0 M KCl), from which the K$^+$ conductance (γ_{K^+}) was determined to be 6.2 ± 0.2 pS. (e) I−V curves recorded in unsymmetrical baths (*cis* chamber = 1.0 M NaCl; *trans* chamber = 1.0 M KCl) for determining K$^+$/Na$^+$ selectivity (P_{K^+}/P_{Na^+}) of **6C6**, which was calculated to be 15.5 using a simplified Goldman−Hodgkin−Katz equation.

involvement of anions in the **6C6**-mediated ion transport process.

Subsequently, we compared the transport rates between K$^+$ and H$^+$ using carbonyl cyanide 4-(trifluoromethoxy) phenylhydrazone (FCCP), which is a known proton carrier. We observed a significant net increase of 14.1% in transport activity mediated by **6C6** in the presence (60.7%) versus the absence (43.1%) of FCCP (Figure 2d). The presence of cooperative action between **6C6** and FCCP indicates that K$^+$ is transported at a faster rate than that of H$^+$.

5(6)-carboxyfluorescein (CF) is a self-quenching fluorescence dye with dimensions of 1.0 nm × 1.0 nm. We entrapped CF dye in the LUVs and found that incorporation of **6C6** at 2 μM into LUVs resulted in no detectable leakage of CF dye (Figure S4). In contrast, melittin, a poreforming toxin with a diameter of 3−4 nm, caused a leakage of 54% and 86% of CF dye at 100 and 200 nM, respectively. These findings confirm the integrity of the LUVs in the presence of **6C6** at 2 μM.

Ion Transport Mechanism Study

To elucidate the potential mechanism responsible for **6C6**-mediated K$^+$ transport, we first investigated the correlation between the observed K$^+$ influx rate constants (K_{obs}) and the concentrations of **6C6**, following an established protocol outlined by Smith and colleagues.[51] The methodology involved preincorporating **6C6** into the EYPC membrane at various concentrations, with subsequent measurement of ion transport activities using the HPTS assay. The preincorporation of **6C6** into the membrane is expected to minimize the influence of the uneven distribution of **6C6** molecules on each side of the membrane. The resulting data, as depicted in Figure 3a, reveals

a linear relationship between K_{obs} and $[\mathbf{6C6}]^2$, implying the requirement of two **6C6** molecules to complete the transmembrane ion transport process.

Is it possible for K$^+$ ions to be transported across the membrane facilitated by **6C6** dimer aggregates? To explore this possibility, we investigated the aggregation behavior of **6C6** in both solution and bilayers, employing UV/vis spectroscopy as a function of the concentration. With an increase in the concentration of **6C6** from 6 to 90 μM— significantly surpassing the EC$_{50}$ value of 0.28 μM for **6C6** in facilitating K$^+$ transport—the UV/vis absorptions at 260 nm in both acetonitrile and bilayers display a linear increase without a discernible shift in the wavelength of maximum absorption, indicating the minimal aggregation of **6C6** in both solutions and bilayers (Figure S5). Next, we constructed two potent H-bonded dimers based on computationally optimized **6C6**, as illustrated in Figure S12.

Evidently, in both dimers, the crown ether units in **6C6** are situated too distant to achieve a cooperative effect. An exploration into the stability of the two potential **6C6** dimers in bilayers, employing molecular dynamics (MD) simulations, reveals their rapid disintegration due to the potential competition of water molecules in intermolecular H-bond formation. Collectively, the prospect of **6C6** facilitating the transport of K$^+$ through H-bonded aggregates can be confidently ruled out.

Furthermore, we prepared the trimethoxy derivative of **6C6**, denoted as **6C6-Me**, which is expected to function as a conventional carrier. The results obtained from the HPTS assay reveal that **6C6-Me** also exhibits the ability to transport K$^+$ and Na$^+$ across the membrane with EC$_{50}$ values of 0.25 and
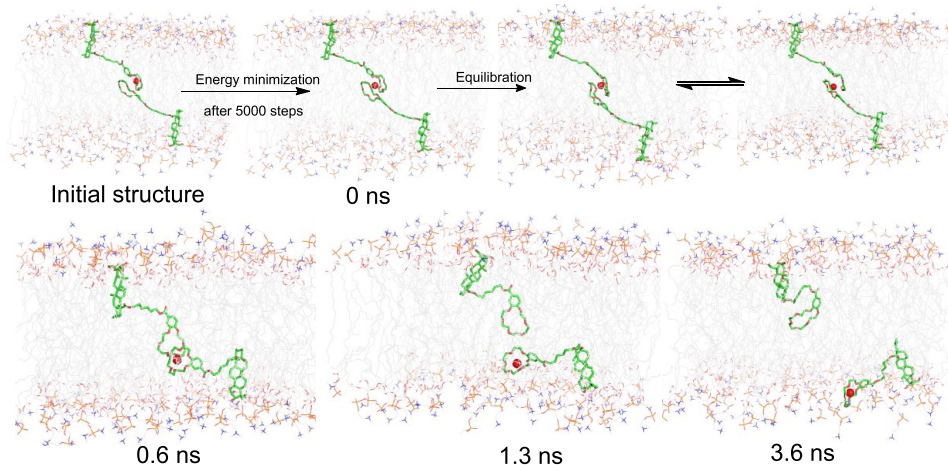
Figure 4. Molecular dynamics (MD) simulation of **6C6**. Molecular dynamics (MD) simulations illustrate the potential K$^+$ ion transport process facilitated by the collaboration of two oppositely arranged **6C6** molecules, with the initial distance between the centers of the two crown ethers set at 3.0 Å. The simulation box comprises 128 POPC molecules and measures 67 Å (width) × 77 Å (width) × 74 Å (height), with 2368 water molecules solvating each side. POPC = 1-palmitoyl-2-oleoyl-*sn*-glycero-3-phosphocholine.

7.8 μM, respectively (Figure S2). Despite **6C6-Me** demonstrating K$^+$ transport activity similar to that of **6C6**, its R_{K^+}/R_{Na^+} value is notably lower at 5.1, sharply contrasting with the observed value of 22.3 for **6C6**. Subsequently, we examined the effect of membrane thickness on the K$^+$ transport activities of both **6C6** and **6C6-Me**. This investigation involved the use of lipid bilayers composed of 1,2-dipalmitoleoyl-*sn*-glycero-3-phosphocholine (16:1 PC), 1-palmitoyl-2-oleoyl-glycero-3-phosphocholine (POPC, 16:0/18:1 PC), and 1,2-dioleoylsn-glycero-3-phosphocholine (18:1 PC), which exhibit increased acyl chain length while sharing the same phosphocholine headgroup. As illustrated in Figure 3b, the K$^+$ transport activity of **6C6** significantly decreases with the increase in membrane thickness. This behavior aligns with the characteristic feature of a relay process involving the collaboration of two molecules, as the hydrophobic gap between the binding units of transporters on the opposite sides of the membrane, introduced by the increased membrane thickness, results in an elevated energetic barrier that hampers the ion transport process.[51,52] Moreover, Figure S7 reveals that increasing cholesterol loading in lipids from 0 to 30 mol % to enhance the membrane rigidity results in a noteworthy reduction in ion transport activity of **6C6**. This observation indicates that the unimpeded mobility of the relay arms is crucial for efficient ion transport. In contrast, the K$^+$ transport activity of **6C6-Me** is independent of the membrane thickness, which is a characteristic of carrier-mediated transport. Collectively, these findings exclude the possibility of **6C6** facilitating K$^+$ transport through a conventional carrier mechanism.

We envisioned that the relay transport of K$^+$ ions by two **6C6** molecules may establish a relatively defined transport pathway and function as an ion channel. To gain more insight into the ion transport mechanism, we conducted planar lipid bilayer experiments in symmetric baths (*cis* chamber = *trans* chamber = 1.0 M KCl). The observation of single-channel current traces at various voltages unambiguously supports the single-channel behavior of **6C6** in transporting ions across the membrane. Also, we observed the presence of numerous sublevel transitions. Collectively, this suggests that the K$^+$ ions are transported through a "motion channel" mechanism, in which K$^+$ ions are transported through numerous stochastic but relatively defined pathways. The K$^+$ ion conductance of

6C6 was determined to be 6.2 pS by linearly fitting the current−voltage (*I*−*V*) plot. Furthermore, we recorded the single-channel current traces for **6C6** in unsymmetrical baths (*cis* chamber = 1.0 M NaCl and *trans* chamber = 1.0 M KCl) to assess the K$^+$/Na$^+$ selectivity (P_{K^+}/P_{Na^+}) (Figure S9). By linear fitting of the *I*−*V* plot in Figure 3e, a reverse potential (ε_{rev}) of 70.3 mV was derived. Using a simplified Goldman−Hodgkin−Katz equation, P_{K^+}/P_{Na^+} was calculated to be 15.5, substantiating the remarkable high selectivity of **6C6** in facilitating the transmembrane transport of K$^+$ ions. Using a similar protocol, the P_{K^+}/P_{Na^+} of **6C8** was determined to be 8.7, which is notably lower than that of **6C6** (Figure S10). This finding aligns with the selectivity trend observed using the R_{K^+}/R_{Na^+} ratio in the HPTS assay and confirms that the ion transport selectivity of transporters is significantly influenced by the length of the side chains.

To unravel the ion transport process at the molecular level, MD simulations using the CHARMM-GUI program,[53] the PME method,[54] and the SHAKE algorithm[55] were conducted. Given the inherent energetic challenges in resolving the initial steps of ion capture from an aqueous medium and its translocation to the membrane center through MD simulations, we focused on elucidating the subsequent steps, including ion relay, swing, and release. Initially, a configuration comprising two oppositely arranged **6C6** molecules, with the upper molecule binding a K$^+$ ion, was embedded within a membrane of 128 POPC molecules, solvated by 2368 water molecules on each side. The distance between the centers of the two crown ethers was set at 5.0 Å. Following a 5000-step energy minimization process, it was observed that the K$^+$ ion remained bound to the upper crown ether (Figure S13a). Throughout the subsequent equilibration process, the K$^+$ ion exhibited highly restricted movement, predominantly in the proximity of the upper crown ether, suggestive of the presence of a significant energetic barrier impeding its transition between the crown ethers. Next, we reduced the distance between the centers of the two crown ethers to 4.0 Å and observed a slight downward movement of the K$^+$ ion after energy minimization, possibly due to the attraction of the lower crown ether (Figure S13b). However, during the equilibration process, the K$^+$ ion could reach only the
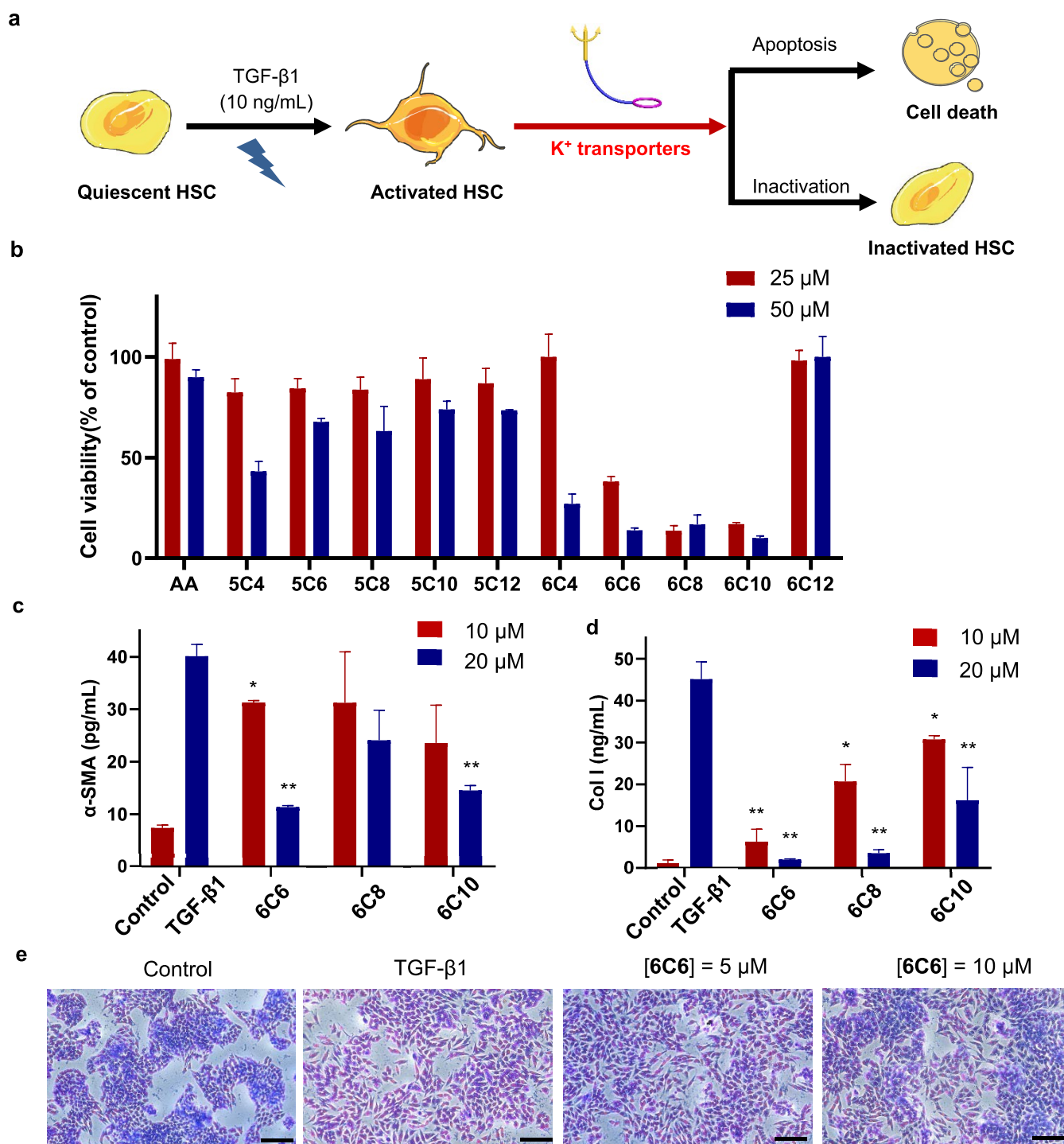
Figure 5. The antiproliferative effect on activated HSCs and inhibition on HSCs activation by ion transporters. (a) Schematic representation of the antihepatic fibrosis strategies using ion transporters. The Figure was partly generated using Servier Medical Art, provided by Servier, licensed under a Creative Commons Attribution 3.0 unported license. (b) Assessment of cell viability in activated HSC-T6 cells upon a 48 h treatment with ion transporters or asiatic acid (**AA**) at 25 and 50 μM by the MTT assay. Evaluation of fibrotic marker proteins α-SMA (c) and Col I (d) in TGF-β1-activated HSC-T6 cells upon a 24 h treatment with ion transporters at 10 and 20 μM. α-SMA = α-smooth muscle actin Col I = Type I collagen (Col I). Results were analyzed and reported as histograms using Graphpad Prism 8.01. Two-tailed Student's t test was used for statistical significance, and data are presented as means $\pm$ SEM ($n = 2$) biologically independent samples. Symbols * and ** stand for significant differences between the control group and other groups, with $p < 0.05$ and 0.01, respectively. (e) Morphological study of TGF-β1-activated HSC-T6 cells upon a 24 h treatment with **6C6** at 5 and 10 μM, respectively. Scale bar: 100 μm.

midpoint between the two crown ethers and was unable to transit to the lower one.

Remarkably, when the distance between the centers of two crown ethers was reduced to 3.0 Å, the K$^+$ ion migrated to the

midpoint between the crown ethers after energy minimization (Figure 4). Throughout the following equilibration process, it was observed that the K$^+$ ion demonstrated the capacity to hop between the crown ethers, indicative of a possible relay process

facilitated by favorable alignment of the crown ethers. These findings suggest that a reduced energetic barrier would result in a more efficient ion transport process between the crown ethers. Next, a 10 ns MD simulation was performed. The simulation trajectories revealed a rapid transfer of the K^+ ion to the lower crown ether. This observation suggests that the state wherein the K^+ ion resides at the midpoint between the two crown ethers lacks stability within a dynamic system. Concomitantly, the **6C6** molecule binding with the K^+ ion underwent a conformational change from an "L" shape to a "U" shape, thereby facilitating the relocation of the K^+ ion from the membrane center to its periphery. In consideration of the symmetric nature of the transporter system and the reversible processes of K^+ ion capture and release, a five-step mechanism for **6C6**-mediated K^+ ion transport is proposed: (i) the capture of the K^+ ion by the crown ether of a **6C6** molecule in the aqueous medium on one side of the membrane; (ii) the swing of the K^+ ion from the periphery to the center of the membrane; (iii) a relay process occurring when the crown ethers of two **6C6** on the opposite side of the membrane are in close proximity; (iv) the swing of the K^+ ion by the other **6C6** molecule to the opposite side of the membrane; and (v) the release of the K^+ ion into the aqueous medium to complete the transmembrane process.

Throughout the simulation, notable stability was observed in the position of free **6C6** on the opposite side of the membrane. As illustrated in Figure S14, a careful examination of the interaction between **6C6** and lipids clearly reveals the presence of intermolecular H-bonds between (i) the H atoms of hydroxyl groups in the asiatic acid and the O atoms of the carbonyl group in POPC, and (ii) the O atoms of hydroxyl groups in the asiatic acid and H atoms of surrounding water molecules. These findings provide further substantiation for the integral role of hydroxyl groups in asiatic acid, acting as lipid anchors.

In Vitro Antihepatic Fibrosis Activity Study

As excessive proliferation and activation of HSCs play a critical role in the progression of liver fibrosis, the approaches for treating liver fibrosis typically involve inducing apoptosis and inactivating HSCs (Figure 5a). In light of the high selectivity and activity of the ion transporters, which hold the potential to perturb intracellularion homeostasis culminating in cellular apoptosis, we initially explored the antiproliferative activity of the transporters on activated HSCs using a rat HSC-T6 cell line. To create an *in vitro* liver fibrosis model, the cells were exposed to TGF-β1 at various concentrations for 24 h. Subsequent quantification of α-smooth muscle actin (α-SMA), a widely acknowledged indicator of fibrosis, revealed successful model creation upon treatment of cells with TGF-β1 at a concentration of 10 ng/mL (Figure S15). Following a 48 h exposure to ion transporters, the cell viability was assessed using a standard MTT assay. As shown in Figure 5b, K^+-selective **6Cn**s generally exhibit greater potency in inhibiting cell proliferation than Na^+-selective **5Cn**s. Specifically, **6C6**, **6C8**, and **6C10** inhibited 86%, 83%, and 90% of activated HSC proliferation at 50 μM, respectively. In contrast, asiatic acid did not demonstrate a noticeable inhibition ability at the same concentration. Encouraged by the potent antiproliferative effects observed with **6C6**, **6C8**, and **6C10**, we conducted a thorough assessment of their selectivity across normal cell lines—specifically, normal hepatic cells (HHL-5), normal kidney cells (HK-2), and normal intestinal cells (HIEC-6)—

compared to activated HSC-T6 cells. As summarized in Table S1 and Figures S16 − S17, the IC_{50} values for **6C6**, **6C8**, and **6C10** against activated HSC-T6 cells were determined to be 14.7, 18.2, and 2.9 μM, respectively. In HHL-5 cells, the corresponding IC_{50} values were found to be 30.2, 21.4, and 4.6 μM. The selectivity indexes (SIs), defined as the ratio of the IC_{50} value in normal cells to that in activated HSC-T6 cells, were calculated to be 2.1, 1.2, and 1.6 for **6C6**, **6C8**, and **6C10**, respectively. Similarly, for HK-2 cells, the SIs were determined to be 1.7, 0.8, and 1.4, and for HIEC-6 cells, they were 1.8, 0.9, and 1.3. Overall, these findings collectively suggest that **6C6** exhibits the most favorable safety profile among the three compounds.

Considering that the efflux of intracellular K^+ could potentially result in the downregulation of TGFβR2 expression, consequently impeding the TGF-β/Smad signaling pathway critical for the activation of HSCs,[2,3,35−38] our subsequent investigation extended to evaluate the potential inhibitory effects of **6C6**, **6C8**, and **610** on HSC activation. α-SMA and Type I collagen (Col I) are expressed at low levels in normal liver HSCs, where they function as fat storage proteins. Upon activation, the expression levels of α-SMA and Col I are upregulated, thereby serving as hallmark indicators of HSC activation. Quantification of the changes in the expression of α-SMA and Col I can provide an effective approach to evaluate the antifibrotic potential of the K^+ transporters. The HSC-T6 cells were activated by TGF-β1 (10 ng/mL), followed by exposure to K^+ transporters at concentrations of 10 and 20 μM for a duration of 24 h, respectively. The expression levels of Col I and α-SMA were quantified using a rapid and sensitive enzyme-linked immunosorbent assay (ELISA). The results presented in Figure 5c,d revealed that activation of HSC-T6 cells with TGF-β1 led to a significant increase in the expression levels of α-SMA and Col I to 40.1 pg/mL and 45.1 ng/mL, respectively. Upon treatment with **6C6**, **6C8**, or **610**, a concentration-dependent reduction in α-SMA and Col I expression levels was observed. Particularly, **6C6** at 20 μM was capable of reducing the expression levels of α-SMA from 40.1 to 11.4 pg/mL and Col I from 45.1 to 2.0 ng/mL. In consideration of its outstanding antiproliferative efficacy, notable inhibitory potential toward HSC activation, and favorable safety profile, **6C6** was selected for further investigation.

HSCs are a type of fibroblast that undergoes transformation into myofibroblast-like cells upon activation by TGF-β1, leading to significant changes in cell morphology. To study the influence of **6C6** on the morphology of HSC-T6 cells, we stained cells with Giemsa solution and captured their morphological characteristics using a microscope. As shown in Figure 5e, upon exposure to TGF-β1, the HSC-T6 cells proliferated rapidly, characterized by enlarged nuclei, loosely arranged and diffusely distributed cells with a shuttle-shaped appearance, and the formation of cytoplasmic extensions resembling fibrous feet, reminiscent of myofibroblasts. However, treating the activated HSCs with **6C6** substantially reduced the number of cells exhibiting elongated fibrous feet and a spindle shape. A majority of the treated cells exhibited a reduced nuclei size and irregularly rounded cell morphology. These observations provided further evidence highlighting the great potential of **6C6** in inhibiting the activation of HSCs.

Given that the activated HSCs exhibit enhanced motility compared to normal HSCs, which is crucial in the pathogenesis of liver fibrosis, the impact of **6C6** on the motility of
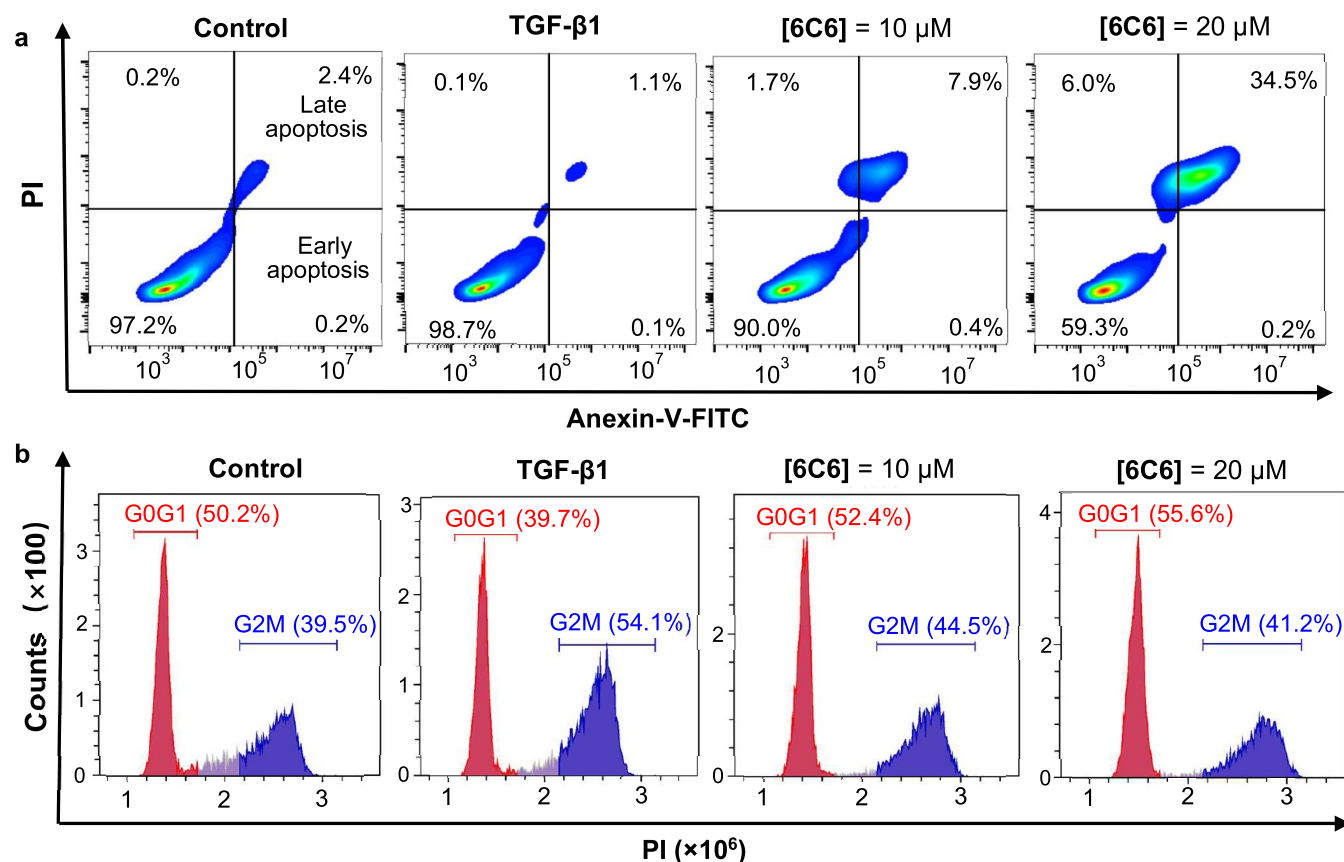
Figure 6. The antiactivated HSC-T6 cell proliferation mechanism study of **6C6**. (a) Evaluation of TGF-β1-activated HSC-T6 cell apoptosis by flow cytometry, with **6C6** at concentrations of 10 and 20 μM for 48 h, respectively, and cells were stained using green Annexin V-FITC conjugate and red PI. Annexin V = intracellular protein of the annexin family that recognizes phosphatidylserines, FITC = fluorescein isothiocyanate, and PI = propidium iodide. (b) Evaluation of TGF-β1-activated HSC-T6 cell cycles by flow cytometry, with **6C6** at concentrations of 10 and 20 μM for 24 h, respectively, and cells were stained using red PI.

HSC-T6 cells was assessed using Transwell assays. Upon treatment with TGF-β1, HSC-T6 cells demonstrated significantly enhanced invasive and migratory abilities. Nevertheless, the significant decrease in the number of invasive and migratory cells, observed in a concentration-dependent manner upon treatment with **6C6** (Figure S18), suggests that **6C6** holds great potential in suppressing the motility of activated HSCs.

To elucidate the mechanism underlying the antiproliferative activity of **6C6** on the activated HSCs, we studied its ability to induce cell apoptosis (Figure 6a) and cell cycle arrest (Figure 6b) using flow cytometry. Due to the antiapoptotic effect of TGF-β1, the TGF-β1 group showed slightly fewer apoptotic cells than the control group. However, when the activated HSC-T6 cells were treated with **6C6** at a concentration of 10 μM, 8.3% cell apoptosis was observed. Further increasing the concentration of **6C6** to 20 μM resulted in a substantial increase in the percentage of cells in apoptosis, reaching 34.7%. These findings unequivocally confirm that **6C6** can promote apoptosis in activated HSCs.

Furthermore, the cell cycle assay revealed that in the control group, 50.2% of HSC-T6 cells were in the G0/G1 phase. TGF-β1 stimulation resulted in cell proliferation, leading to a significant reduction in the percentage of cells in the G0/G1 phase to 39.7%. Notably, treatment with 10 μM of **6C6** caused a significant increase in the percentage of cells in the G0/G1 phase to 52.4%. An increased proportion of HSC-T6 cells in

the G0/G1 phase was observed upon the treatment with **6C6** at a concentration of 20 μM, indicating that the antiproliferative effect of **6C6** on activated HSC-T6 cell proliferation is concomitant with the arrest of the cell cycle in the G0/G1 phase.

To unveil the potential mechanism underlying the inhibitory effect on the HSC activation mediated by **6C6**, which may involve the highly active and selective efflux of intracellular K$^+$ and subsequent downregulation of TGFβR2, we performed an initial investigation using Enhanced Potassium Green-2 AM (EPG-AM), a fluorescence-enhanced K$^+$ probe, to monitor the changes in intracellular K$^+$ level. The fluorescence intensity of HSC-T6 cells was analyzed by using flow cytometry, revealing that the untreated cells exhibited the highest fluorescence intensity (Figure 7a). Exposure to **6C6** resulted in a marked decrease in the fluorescence intensity of HSC-T6 cells, exhibiting a concentration-dependent manner. The impact of **6C6** on the intracellular K$^+$ concentration in HSC-T6 cells was further validated using confocal microscopy, as illustrated in Figure 7b. The results demonstrate that **6C6** exerted a significant downregulatory effect on intracellular K$^+$ concentration.

Given the close correlation between the intracellular K$^+$ concentration and the expression of TGFβR2, we sought to investigate whether **6C6** could influence the expression of TGFβR2 and the downstream TGF-β/Smad signaling pathway. It is reported that when TGF-β1 binds to TGFβR2, it
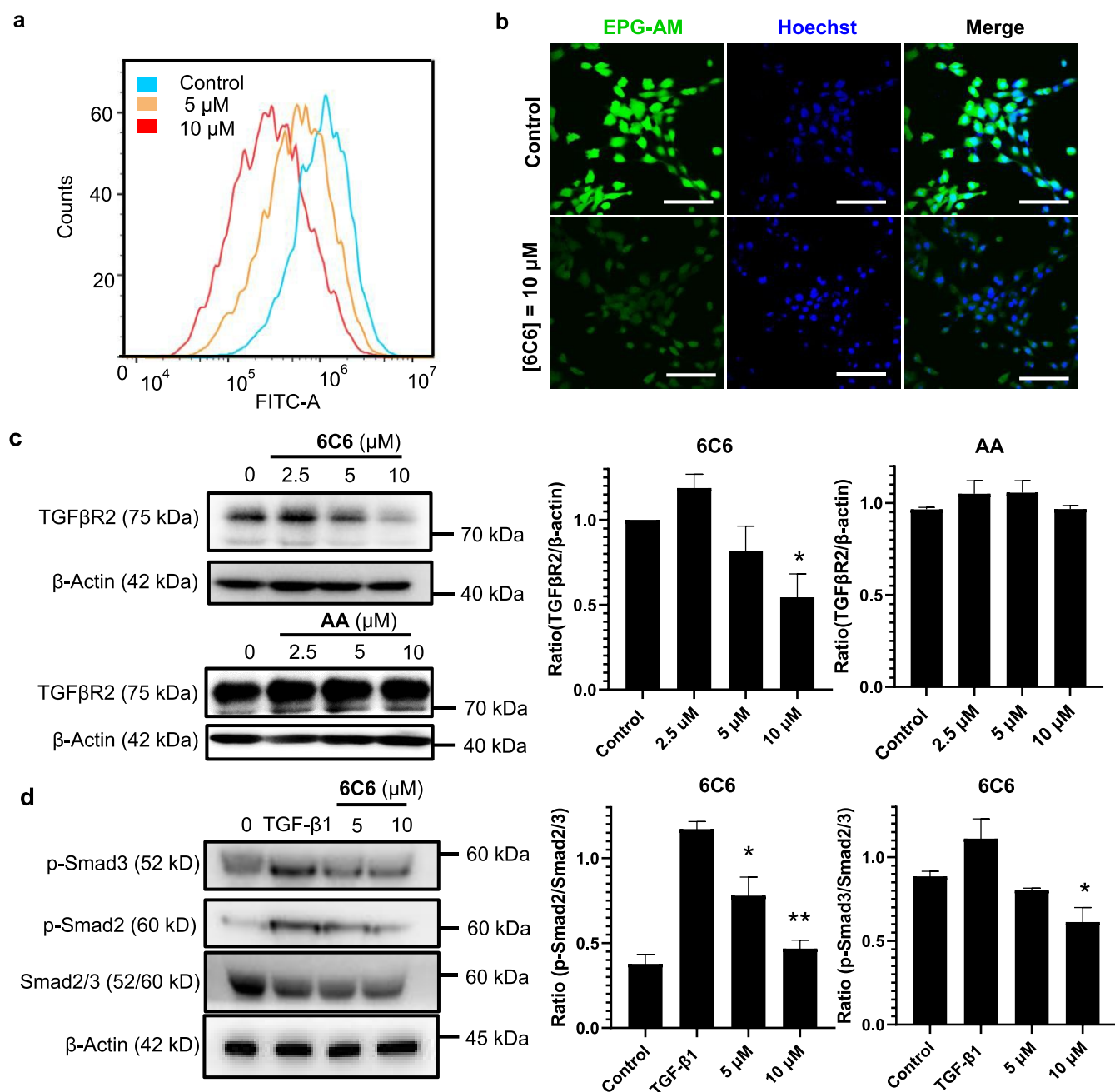
Figure 7. The anti-HSC-T6 cell activation mechanistic study of 6C6. (a) Evaluation of the intracellular K^+ levels in HSC-T6 cells upon a 6-h treatment of **6C6** at concentrations of 5 μM and 10 μM by flow cytometry. The cells were stained with the green K^+ probes EPG-AM (λ_{ex} = 488 nm, λ_{em} = 540 nm). EPG-AM = Enhanced Potassium Green-2 AM. (b) Evaluation of intracellular K^+ levels in HSC-T6 cells upon a 6-h treatment of **6C6** at a concentration of 10 μM by confocal microscopy. Scale bar: 20 μm. (c) Immunoblot assay for quantification of TGFβR2 in HSC-T6 cells upon a 12 h treatment of up to 10 μM **6C6** and **AA**. (d) Immunoblot assay for quantification of Smad2/3, p-Smad2, and p-Smad3 in TGF-β1-activated HSC-T6 cells upon a 24 h treatment of up to 10 μM of **6C6**. The results were analyzed by ImageJ 1.8.0. Two-tailed Student's t test was used for statistical significance, and data are presented as means $\pm$ SEM (n = 2) biologically independent samples. Symbols * and ** stand for significant differences between the control group and other groups, with $p < 0.05$ and 0.01, respectively. The uncropped images of the gels in this figure are provided in Figure S20.

triggers the formation of a complex with TGFβR1, leading to the phosphorylation of Smad proteins. The phosphorylated Smad proteins subsequently interact with Co-Smad and translocate into the nucleus to regulate gene transcription, ultimately driving fibroblast activation.[56] We examined the effect of **6C6** on the expression of TGFβR2 and downstream key pathway proteins, including p-Smad2 and p-Smad3 in HSC-T6 cells by immunoblot assays. The results illustrated in

Figure 7c exhibited a dose-dependent reduction in the expression of TGFβR2 when HSC-T6 cells were treated with **6C6**. On the contrary, the anchoring component asiatic acid was incapable of affecting the TGFβR2 expression. This sharp contrast can be attributed to the exceptional ability of **6C6** to modulate intracellular K^+ concentration, a characteristic not observed in the case of asiatic acid. As a consequence of the downregulation of TGFβR2, the phosphorylation of Smad2
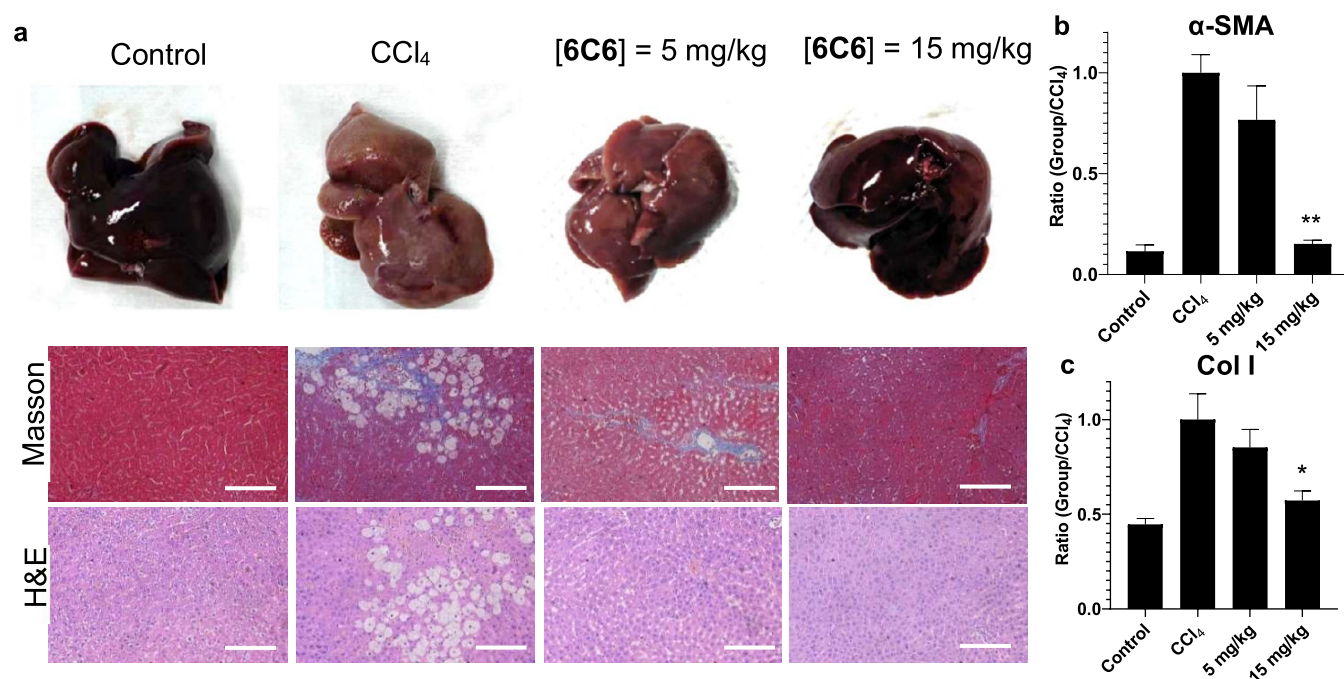
Figure 8. The *in vivo* antihepatic fibrosis activity study of **6C6**. (a) Representative gross morphology and histopathological analysis of rat liver samples. Scale bar: 100 μm. Evaluation of (b) α-SMA and (c) Col I levels in CCl$_4$-induced hepatic fibrosis rats treated with **6C6** (5 and 15 mg/kg) by enzyme-linked immunosorbent assay (ELISA). The results were analyzed by Graphpad Prism 8.01. Two-tailed student's *t* test was used for statistical significance, and data are presented as means $\pm$ SEM ($n = 3$) biologically independent samples. Symbols * and ** stand for significant differences between the CCl$_4$ group and other groups, with $p < 0.05$ and 0.01, respectively.

and Smad3 mediated by TGF-β1 was significantly attenuated upon treatment with **6C6** (Figure 7d). These findings confirm that the highly active and selective efflux of K$^+$ mediated by **6C6** is capable of inducing downregulation in the expression of TGFβR2, subsequently impeding the downstream TGF-β/Smad signaling cascade, which may account for its prominent efficacy in inhibiting the activation of HSCs.

In Vivo Antihepatic Fibrosis Activity Study

The impressive *in vitro* antifibrotic activity and low acute toxicity (LD$_{50}$ > 150 mg/kg) of **6C6** prompted us to further explore the *in vivo* protective effect of **6C6** against liver fibrosis. A liver fibrosis rat model was prepared through the injection of CCl$_4$ at a concentration of 2 mL/kg twice a week over a period of 4 weeks. The successful induction of liver fibrosis was confirmed by the observation of significantly elevated α-SMA and Col I levels in the tissues of the CCl$_4$-treated model group. Next, rats were administered with **6C6** continuously at doses of 5 and 15 mg/kg over a period of 2 weeks, respectively. Following treatment with **6C6**, significant changes in the morphology of the rat liver were observed. The liver in the CCl$_4$-treated group exhibited prominent fibrosis, presenting a granular surface, a pale color, and enlarged tissue size. In contrast, treatment with **6C6** at a dose of 15 mg/kg resulted in a smooth liver surface with a dark red color and no significant enlargement in size, resembling the morphological characteristics observed in the control group (Figure 8a). Changes in fibrosis markers, such as α-SMA and Col I, in rat liver tissue were subsequently assessed to evaluate the antifibrotic effect of **6C6**. As depicted in Figure 8b,c, the group treated with a high dose of **6C6** demonstrated a substantial reduction in the α-SMA and Col I levels, providing compelling evidence for the potential of **6C6** to ameliorate liver fibrosis *in vivo*.

Analysis of pathological tissue sections using Masson's Trichrome staining and hematoxylin and eosin (H&E) staining provided additional insights into the morphological alterations occurring in the liver tissue. As shown in Figure 8a, in the control group, the liver lobules exhibited an intact structural morphology, characterized by orderly arranged hepatocytes, without discernible signs of fatty degeneration, infiltration of inflammatory cells, or cell necrosis. However, within the CCl$_4$-treated model group, a disruption in the organization of cellular structures, substantial tissue breakage, fatty degeneration, and infiltration of inflammatory cells was observed, accompanied by the occurrence of hepatocyte necrosis. Moreover, the result from Masson's Trichrome staining demonstrated a marked elevation in collagen deposition, as evidenced by the notable increase in the blue staining fraction. Excitingly, treatment with **6C6** gave rise to a dose-dependent reduction in collagen deposition along with significant improvement in the morphology of the liver lobules. Upon treatment with **6C6** at a concentration of 15 mg/kg, a considerable majority of hepatocytes exhibited intact cellular structures, accompanied by the absence of infiltration of inflammatory cells or fat vacuoles. Moreover, H&E staining was performed on the kidneys and spleens of rats to evaluate the potential toxicity associated with continuous administration of **6C6**. As revealed in Figure S21, both the kidney and spleen cells within the two administration groups exhibited closely arranged and intact cellular structures, with no notable lesions or abnormalities observed. These observations indicate the low toxicity of **6C6** at the administered doses, up to 15 mg/kg. Collectively, these findings highlight the outstanding efficacy of **6C6** in preserving the structural integrity of hepatocytes and mitigating the infiltration of inflammatory cells and fat vacuoles, thereby emphasizing the significant

promise of **6C6** as a novel therapeutic candidate for the treatment of liver fibrosis.

CONCLUSIONS

In conclusion, we have successfully developed an unconventional class of highly active and selective K$^+$ transporters involving the motional collaboration of two K$^+$ ion transporters. In particular, **6C6** demonstrates impressive K$^+$ transport activity and selectivity, as evidenced by its low EC$_{50}$ value of 0.28 μM (0.28 mol % relative to lipid) and high K$^+$/Na$^+$ selectivity of 15.5, which is undoubtedly among the most selective K$^+$ transporters in the open literature. Significantly, our work, for the first time, demonstrates the potent antihepatic fibrosis effects of **6C6** both *in vitro* and *in vivo*. The antifibrotic effects of **6C6** are achieved through a combination of multiple mechanisms, including the induction of apoptosis and the arrest of the cell cycle progression within activated HSCs, as well as the inhibition of HSC activation. This work not only expands the repertoire of highly active and selective artificial K$^+$ transporters but also marks a significant milestone for the application of artificial K$^+$ transporters as potent therapeutics for the treatment of diseases associated with the dysregulation of K$^+$ ion transport.

MATERIALS AND METHODS

Materials

Egg yolk L-α-phosphatidylcholin (EYPC) was purchased from Avanti Polar Lipids. Fetal bovine serum (FBS), penicillin−streptomycin, RPMI-1640 medium, and Dulbecco's modified Eagle's medium (DMEM) were obtained from Hyclone. FITC-Annexin-V, PI solution, and RNase A were purchased from Yeasen. Enhanced Potassium Green-2 AM (EPG-2 AM) was purchased from Shanghai Maokang Biotechnology Co., Ltd. (China). All of the ELISA kits were obtained from Elabscience Biotechnology Co., Ltd. Hoechst staining solution, Jimesa staining solution, and EDTA were purchased from Solarbio. Polyvinylidene fluoride (PVDF) was obtained from Millipore. TGFβR2 pAb and peroxidase-conjugated secondary antibody solution were purchased from Abcam; Smad2/3 pAb, p-Smad2 pAb, p-Smad3 pA, and β-actin pAb were purchased from Abclonal. Pierce ECL Western Blotting Substrate was obtained from Thermo Scientific.

Ion Transport Study Using HPTS Assay

25.0 mg of Egg yolk L-α-phosphatidylcholin (EYPC, Avanti Polar Lipids) was dissolved in 1.0 mL of CHCl$_3$ in a round-bottom flask. Removal of CHCl$_3$ under reduced pressure at 35 °C resulted in a thin film, which was subjected to high vacuum overnight at 25 °C. The resulting film was hydrated with a 1.0 mL solution of HEPES buffer (10 mM HEPES, 100 mM NaCl, pH = 7.0) containing pH-sensitive dye HPTS (1.0 mM). The hydration process was performed using an orbital shaker at 25 °C for 1 h, resulting in the formation of a milky suspension.

The suspension was subjected to 10 freeze−thaw cycles, involving freezing in liquid N$_2$ for 60 s, followed by heating at 55 °C for 120 s. To obtain a homogeneous suspension of large unilamellar vesicles (LUVs) with HPTS encapsulated inside, the vesicle suspension was extruded 21 times through a polycarbonate membrane (0.1 μm). Separation of the unencapsulated HPTS from LUVs was achieved by using size exclusion chromatography. The stationary phase consisted of Sephadex G-50 (GE Healthcare), while the mobile phase consisted of 10 mM HEPES and 100 mM NaCl at pH = 7.0. The collected LUV solution was then diluted with the mobile phase to yield a stock solution of 6.5 mM.

For the ion transport study, 30 μL of the HPTS-containing LUV stock solution was added to a HEPES buffer solution (1.95 mL, 10 mM HEPES, 100 mM NaCl, pH = 8.0) in order to create a pH gradient. Subsequently, a solution of ion transporters in dimethyl sulfoxide (DMSO) was injected into the suspension with gentle stirring. The emission of HPTS was immediately recorded at 510 nm with excitations at both 460 and 403 nm for a duration of 300 s by using a fluorescence spectrophotometer (Hitachi, Model F-7100, Japan). At 300 s, 20 μL of Triton X-100 (20% v/v) was added to induce the maximum change in the fluorescence dye emission. The final transport trace was obtained by calculating the ratiometric value of I_{460}/I_{403} and normalizing it based on the ratiometric value of I_{460}/I_{403} after the addition of Triton, using eq 1.

$$I_f = (I_t - I_0)/(I_1 - I_0) \tag{1}$$

where I_f = fractional emission intensity, I_t = fluorescence intensity at time t, I_1 = fluorescence intensity after addition of Triton X-100, and I_0 = initial fluorescence intensity.

Fitting the fractional ion transport activity R versus ion transporter concentration using Hill eq 2 gave the EC$_{50}$ values and the Hill coefficient n.

$$R = 1/(1 + (EC_{50}/[\text{ion transporter}])^n) \tag{2}$$

where R = fractional ion transport activity.

Single-Channel Conductance Measurement Using Planar Lipid Bilayer System

The chloroform solution containing a mixture of **6C6** (11.8 μM, 40 μL) and 1,2-diphytanoyl-*sn*-glycero-3-phosphocholine (diPhyPC, 10 mg/mL, 40 μL) was evaporated using nitrogen gas to form a thin film and redissolved in *n*-decane (16 μL). 0.5 μL of this *n*-decane solution was injected into the aperture of the Delrin cup (Warner Instruments, Hamden, CT) with the *n*-decane removed using nitrogen gas. In a typical experiment, both the chamber (*cis* side) and Delrin cup (*trans* side) were filled with an aqueous KCl solution. Ag-AgCl electrodes were inserted into the two solutions, with the *cis* chamber grounded. A planar lipid bilayer was formed by painting 0.3 μL of the lipid-containing *n*-decane solution around the *n*-decane-pretreated aperture. The single-channel currents were then measured using a Warner BC-535D bilayer clamp amplifier, collected by PatchMaster (HEKA) with a sample interval at 5 kHz and filtered with an 8-pole Bessel filter at 1 kHz (HEKA). The data were analyzed by FitMaster (HEKA) with a digital filter at 100 Hz. Plotting current traces vs voltages yielded ion conductance (γ). For the transport selectivity of K$^+$ over Na$^+$, the *cis* chamber was filled with 1.0 M NaCl, and the *trans* chamber was filled with 1.0 M KCl. The single-channel currents at different voltages were recorded following the same protocol as mentioned above.

Growth Inhibition of Activated HSCs Using MTT Assay

HSC-T6 cells or normal hepatic cells (HHL-5 cell line) were cultured in Dulbecco's modified Eagle medium (DMEM, Hyclone) containing 10% of fetal bovine serum (FBS) and 10,000 U/mL of Penicillin−Streptomycin at 37 °C in a humidified atmosphere containing 5% CO$_2$. HSC-T6 cells were seeded into 96-well plates with a cell density of 5 × 10^3 cells/well in 200 μL of DMEM medium. After incubation for 12 h, HSC-T6 cells were activated with TGF-β1 (10 ng/mL) for 24 h. Ion transporters or asiatic acid at a final concentration of 25 and 50 μM were added into the culture medium, respectively, to incubate with cells for another 48 h. Next, the medium was replaced with MTT solution (free DMEM as solvent, 500 μg/mL). After incubation for another 4 h, the medium in the 96-well plate was removed, and 150 μL of DMSO was added. The whole well plates were shaken to completely dissolve the purple formazan crystals. UV-absorption at 490 nm was recorded by an absorbance microplate reader (CMAX PLUS, Molecular Devices). Cell viabilities upon the addition of compounds at various concentrations were calculated, following eq 3. The IC$_{50}$ values of **6C6, 6C8, and 6C10** against activated HSC-T6 cells were calculated using a nonlinear regression curve fit with Graphpad Prism 8.0.1.

$$\% \text{ cell viability} = (OD_{490}(\text{ion transporters})/OD_{490}(0.5\% \text{ DMSO}))$$
$$\times 100\% \tag{3}$$

The IC_{50} values of **6C6**, **6C8**, and **6C10** against cells were obtained by fitting growth curves in Graphpad Prism 8.0.1, employing the 'log(inhibitor) vs response—Viable slope (four parameters) eq 4.

$$Y = Y_0 + (Y_1 - Y)_0/(1 + 10^{\wedge}((\text{Log IC}_{50} - X)K)) \quad (4)$$

where X = logarithm of the concentration of ion transporter and K = steepness of the family of curves. Y_1 = Top plateaus in units of the Y axis. Y_0 = bottom plateaus in units of the Y axis.

ELISA Assay for Determining α-SMA and Col I

HSC-T6 cells were seeded into 6-well plates at a density of 2.5×10^5 cells/mL. After 12 h, HSC-T6 cells were stimulated with 10 ng/mL of TGF-β1, and ion transporters were added at concentrations of 0, 10, and 20 μM, respectively. After incubation for 24 h, the cells were lysed with NP40, and the supernatant was collected after centrifugation (1120g) for 10 min. The protein concentrations were determined by a BCA kit (Solarbio, China). The expression of Col I and α-SMA was measured by using an ELISA kit (Elabscience Biotechnology Co., Ltd.). Samples were added in ELISA microplates and incubated for 60 min at 37 °C. Then, horseradish peroxidase (HRP) solution was added and incubated for 30 min. After incubation, the microplates were washed with 1× wash buffer 5 times. Subsequently, Solution A and Solution B in the ELISA kit were added into each well and incubated for 15 min at 37 °C. The reaction was terminated by the stop solution in the ELISA kit. The OD values at 450 nm were recorded by an absorbance microplate reader (CMAX PLUS, Molecular Devices).

Inhibitory Effects of 6C6 on CCl₄-Induced Hepatic Fibrosis in Rats

All animal study protocols were in compliance with the principles and procedures that were defined in the Guide for the Care and Use of Laboratory Animals, approved by the Institutional Animal Care and Use Committee of Xiamen University (NO. XMULAC20200029). Male Wistar rats weighing 180 ± 10 g were randomly assigned to four groups: (i) control group (n = 3), which received intraperitoneal administration of olive oil at a dosage of 2 mL/kg twice a week for a duration of 4 weeks; (ii) CCl₄-treated group (n = 3); (iii) low-dose administration group (5 mg/kg b.w.); and (iv) high-dose administration group (15 mg/kg b.w.). The CCl₄ group, low-dose administration group, and high-dose administration group were treated with CCl₄ (40% in olive oil) twice a week at a dosage of 2 mL/kg through intraperitoneal injection for a period of 4 weeks. Next, **6C6** (5 and 15 mg/kg) was administered to the rats via intraperitoneal injection daily for a duration of 2 weeks. Rats were euthanized after 2 weeks by CO₂ inhalation, and the selected organs were removed, frozen using liquid N₂, and stored at −80 °C for further analysis.

Statistical Analysis

All data were presented as mean ± standard deviation, and ANOVA t test was used for significance analysis between the two groups. The P-value below 0.05 was considered as significant difference, where *P < 0.05; **P < 0.01.

■ ASSOCIATED CONTENT

Ⓢ Supporting Information

The Supporting Information is available free of charge at https://pubs.acs.org/doi/10.1021/jacsau.4c00521.

> Synthetic procedures and a full set of characterization data, including ¹H NMR, ¹³C NMR, MS, ion transport studies, and biological studies (PDF)
> Molecular dynamic simulations (AVI)

■ AUTHOR INFORMATION

Corresponding Author

Changliang Ren − *State Key Laboratory of Cellular Stress Biology and Fujian Provincial Key Laboratory of Innovative Drug Target Research, School of Pharmaceutical Sciences, Xiamen University, Xiamen, Fujian 361102, China; Shenzhen Research Institute of Xiamen University, Shenzhen, Guangdong 518057, China;* ⓞ orcid.org/0000-0003-2657-9412; Email: changliang.ren@xmu.edu.cn

Authors

Qiuping Zhang − *State Key Laboratory of Cellular Stress Biology and Fujian Provincial Key Laboratory of Innovative Drug Target Research, School of Pharmaceutical Sciences, Xiamen University, Xiamen, Fujian 361102, China; Shenzhen Research Institute of Xiamen University, Shenzhen, Guangdong 518057, China*

Qinghong Liang − *State Key Laboratory of Cellular Stress Biology and Fujian Provincial Key Laboratory of Innovative Drug Target Research, School of Pharmaceutical Sciences, Xiamen University, Xiamen, Fujian 361102, China; Shenzhen Research Institute of Xiamen University, Shenzhen, Guangdong 518057, China*

Guijiang Wang − *State Key Laboratory of Cellular Stress Biology and Fujian Provincial Key Laboratory of Innovative Drug Target Research, School of Pharmaceutical Sciences, Xiamen University, Xiamen, Fujian 361102, China*

Xiaopan Xie − *State Key Laboratory of Cellular Stress Biology and Fujian Provincial Key Laboratory of Innovative Drug Target Research, School of Pharmaceutical Sciences, Xiamen University, Xiamen, Fujian 361102, China*

Yin Cao − *State Key Laboratory of Cellular Stress Biology and Fujian Provincial Key Laboratory of Innovative Drug Target Research, School of Pharmaceutical Sciences, Xiamen University, Xiamen, Fujian 361102, China*

Nan Sheng − *State Key Laboratory of Cellular Stress Biology and Fujian Provincial Key Laboratory of Innovative Drug Target Research, School of Pharmaceutical Sciences, Xiamen University, Xiamen, Fujian 361102, China*

Zhiping Zeng − *State Key Laboratory of Cellular Stress Biology and Fujian Provincial Key Laboratory of Innovative Drug Target Research, School of Pharmaceutical Sciences, Xiamen University, Xiamen, Fujian 361102, China*

Complete contact information is available at: https://pubs.acs.org/10.1021/jacsau.4c00521

Author Contributions

CRediT: **Qiuping Zhang** data curation, formal analysis, investigation, methodology, validation; **Qinghong Liang** data curation, investigation, validation; **Guijiang Wang** data curation, investigation, visualization; **Xiaopan Xie** data curation, investigation, validation; **Yin Cao** data curation, investigation, validation; **Nan Sheng** data curation, investigation, validation; **Zhiping Zeng** data curation, formal analysis, investigation, methodology, visualization; **Changliang Ren** conceptualization, funding acquisition, project administration, resources, supervision, writing-original draft, writing-review & editing.

Notes

The authors declare no competing financial interest.

■ ACKNOWLEDGMENTS

■ REFERENCES

(1) Eisenberg, B. Ionic channels in biological membranes: natural nanotubes. *Acc. Chem. Res.* **1998**, *31* (3), 117−124.

(2) Orlov, S. N.; La, J.; Smolyaninova, L. V.; Dulin, N. O. Na⁺, K⁺-ATPase as a target for treatment of tissue fibrosis. *Curr. Med. Chem.* **2019**, *26* (3), 564−575.

(3) Yang, L.; Han, B.; Zhang, M.; Wang, Y.-H.; Tao, K.; Zhu, M. X.; He, K.; Zhang, Z.-G.; Hou, S. Activation of BK channels prevents hepatic stellate cell activation and liver fibrosis through the suppression of TGFβ1/SMAD3 and JAK/STAT3 profibrotic signaling pathways. *Front. Pharmacol.* **2020**, *11*, 165.

(4) Pardo, L. A.; Stühmer, W. The roles of K⁺ channels in cancer. *Nat. Rev. Cancer* **2014**, *14* (1), 39−48.

(5) Shima, N.; Yamamura, A.; Fujiwara, M.; Amano, T.; Matsumoto, K.; Sekine, T.; Okano, H.; Kondo, R.; Suzuki, Y.; Yamamura, H. Up-regulated expression of two-pore domain K⁺ channels, KCNK1 and KCNK2, is involved in the proliferation and migration of pulmonary arterial smooth muscle cells in pulmonary arterial hypertension. *Front Cardiovasc. Med.* **2024**, *11*, No. 1343804.

(6) Yuan, X.; Shen, J.; Zeng, H. Artificial transmembrane potassium transporters: designs, functions, mechanisms and applications. *Chem. Commun.* **2024**, *60*, 482−500.

(7) Kim, D. M.; Nimigean, C. M. Voltage-gated potassium channels: a structural examination of selectivity and gating. *Cold Spring Harb. Perspect. Biol.* **2016**, *8* (5), No. a029231.

(8) Ren, C.; Shen, J.; Zeng, H. Combinatorial evolution of fast-conducting highly selective K⁺-channels via modularly tunable directional assembly of crown ethers. *J. Am. Chem. Soc.* **2017**, *139* (36), 12338−12341.

(9) Barboiu, M. Encapsulation versus self-aggregation toward highly selective artificial K⁺ channels. *Acc. Chem. Res.* **2018**, *51* (11), 2711−2718.

(10) Jin, L.; Sun, C.; Li, Z.; Shen, J.; Zeng, H. A K⁺-selective channel with a record-high K⁺/Na⁺ selectivity of 20.1. *Chem. Commun.* **2023**, *59* (24), 3610−3613.

(11) Ma, H.; Ye, R.; Jin, L.; Zhou, S.; Ren, C.; Ren, H.; Shen, J.; Zeng, H. Highly active artificial potassium channels having record-high K⁺/Na⁺ selectivity of 20.1. *Chin. Chem. Lett.* **2023**, *34*, No. 108355.

(12) Qiao, D.; Joshi, H.; Zhu, H.; Wang, F.; Xu, Y.; Gao, J.; Huang, F.; Aksimentiev, A.; Feng, J. Synthetic macrocycle nanopore for potassium-selective transmembrane transport. *J. Am. Chem. Soc.* **2021**, *143* (39), 15975−15983.

(13) Qi, S.; Zhang, C.; Yu, H.; Zhang, J.; Yan, T.; Lin, Z.; Yang, B.; Dong, Z. Foldamer-based potassium channels with high ion selectivity and transport activity. *J. Am. Chem. Soc.* **2021**, *143* (9), 3284−3288.

(14) Lang, C.; Deng, X.; Yang, F.; Yang, B.; Wang, W.; Qi, S.; Zhang, X.; Zhang, C.; Dong, Z.; Liu, J. Highly selective artificial potassium ion channels constructed from pore-containing helical oligomers. *Angew. Chem., Int. Ed.* **2017**, *56* (41), 12668−12671.

(15) Chen, F.; Shen, J.; Li, N.; Roy, A.; Ye, R.; Ren, C.; Zeng, H. Pyridine/Oxadiazole-based helical foldamer ion channels with exceptionally high K⁺/Na⁺ selectivity. *Angew. Chem., Int. Ed.* **2020**, *59* (4), 1440−1444.

(16) Ding, B.-S.; Cao, Z.; Lis, R.; Nolan, D. J.; Guo, P.; Simons, M.; Penfold, M. E.; Shido, K.; Rabbany, S. Y.; Rafii, S. Divergent angiocrine signals from vascular niche balance liver regeneration and fibrosis. *Nature* **2014**, *505* (7481), 97−102.

(17) Afdhal, N. H.; Nunes, D. Evaluation of liver fibrosis: a concise review. *Am. J. Gastroenterol.* **2004**, *99* (6), 1160−1174.

(18) Hernandez-Gea, V.; Friedman, S. L. Pathogenesis of liver fibrosis. *Annu. Rev. Pathol.* **2011**, *6*, 425−456.

(19) Tsukada, S.; Parsons, C. J.; Rippe, R. A. Mechanisms of liver fibrosis. *Clin. Chim. Acta* **2006**, *364* (1−2), 33−60.

(20) Gutiérrez-Ruiz, M. C.; Gómez-Quiroz, L. E. Liver fibrosis: searching for cell model answers. *Liver Int.* **2007**, *27* (4), 434−439.

(21) Lurie, Y.; Webb, M.; Cytter-Kuint, R.; Shteingart, S.; Lederkremer, G. Z. Non-invasive diagnosis of liver fibrosis and cirrhosis. *World J. Gastroenterol.* **2015**, *21* (41), 11567.

(22) Han, K.-H.; Yoon, K. T. New diagnostic method for liver fibrosis and cirrhosis. *Intervirology* **2008**, *51* (Suppl. 1), 11−16.

(23) Dhar, D.; Baglieri, J.; Kisseleva, T.; Brenner, D. A. Mechanisms of liver fibrosis and its role in liver cancer. *Exp. Biol. Med.* **2020**, *245* (2), 96−108.

(24) Affo, S.; Yu, L.-X.; Schwabe, R. F. The role of cancer-associated fibroblasts and fibrosis in liver cancer. *Annu. Rev. Pathol.* **2017**, *12*, 153−186.

(25) Roehlen, N.; Crouchet, E.; Baumert, T. F. Liver fibrosis: mechanistic concepts and therapeutic perspectives. *Cell* **2020**, *9* (4), 875.

(26) Tan, Z.; Sun, H.; Xue, T.; Gan, C.; Liu, H.; Xie, Y.; Yao, Y.; Ye, T. Liver fibrosis: therapeutic targets and advances in drug therapy. *Front. Cell Dev. Biol.* **2021**, *9*, No. 730176.

(27) Wu, J.; Zern, M. A. Hepatic stellate cells: a target for the treatment of liver fibrosis. *J. Gastroenterol.* **2000**, *35*, 665−672.

(28) Seki, E.; Schwabe, R. F. Hepatic inflammation and fibrosis: functional links and key pathways. *Hepatology* **2015**, *61* (3), 1066−1079.

(29) Meindl-Beinker, N. M.; Dooley, S. Transforming growth factor-β and hepatocyte transdifferentiation in liver fibrogenesis. *J. Gastroenterol. Hepatol.* **2008**, *23*, S122−S127.

(30) Inagaki, Y.; Okazaki, I. Emerging insights into transforming growth factor β Smad signal in hepatic fibrogenesis. *Gut* **2007**, *56* (2), 284−292.

(31) Derynck, R.; Zhang, Y. E. Smad-dependent and Smad-independent pathways in TGF-β family signalling. *Nature* **2003**, *425* (6958), 577−584.

(32) Sanjabi, S.; Zenewicz, L. A.; Kamanaka, M.; Flavell, R. A. Anti-inflammatory and pro-inflammatory roles of TGF-β, IL-10, and IL-22 in immunity and autoimmunity. *Curr. Opin. Pharmacol.* **2009**, *9* (4), 447−453.

(33) Massagué, J. TGFβ in cancer. *Cell* **2008**, *134* (2), 215−230.

(34) Shi, N.; Wang, Z.; Zhu, H.; Liu, W.; Zhao, M.; Jiang, X.; Zhao, J.; Ren, C.; Zhang, Y.; Luo, L. Research progress on drugs targeting the TGF-β signaling pathway in fibrotic diseases. *Immunol. Res.* **2022**, *70* (3), 276−288.

(35) La, J.; Reed, E.; Chan, L.; Smolyaninova, L. V.; Akomova, O. A.; Mutlu, G. M.; Orlov, S. N.; Dulin, N. O. Downregulation of TGF-β receptor-2 expression and signaling through inhibition of Na/K-ATPase. *PLoS One* **2016**, *11* (12), No. e0168363.

(36) Wang, Y.; Wang, M.; Ning, F.; Ren, D.; Tao, J.; Xie, W.; Eaton, D. C.; Jiang, G.; Farris, A. B.; Xin, H.; et al. A novel role of BK potassium channel activity in preventing the development of kidney fibrosis. *Kidney Int.* **2022**, *101* (5), 945−962.

(37) Bengtson, C. D.; Kim, M. D.; Anabtawi, A.; He, J.; Dennis, J. S.; Miller, S.; Yoshida, M.; Baumlin, N.; Salathe, M. Hyperglycaemia in cystic fibrosis adversely affects BK channel function critical for mucus clearance. *Eur. Respir. J.* **2020**, *57* (1), No. 2000509.

(38) Xu, H.; Garver, H.; Fernandes, R.; Phelps, J. T.; Harkema, J. J.; Galligan, J. J.; Fink, G. D. BK channel β1-subunit deficiency exacerbates vascular fibrosis and remodeling but does not promote hypertension in high fat fed obesity in mice. *J. Hypertens.* **2015**, *33* (8), 1611.

(39) Shen, J.; Ren, C.; Zeng, H. Membrane-active molecular machines. *Acc. Chem. Res.* **2022**, *55* (8), 1148−1159.

(40) Johnson, T. G.; Langton, M. J. Molecular machines for the control of transmembrane transport. *J. Am. Chem. Soc.* **2023**, *145* (50), 27167−27184.

(41) García-López, V.; Chen, F.; Nilewski, L. G.; Duret, G.; Aliyan, A.; Kolomeisky, A. B.; Robinson, J. T.; Wang, G.; Pal, R.; Tour, J. M. Molecular machines open cell membranes. *Nature* **2017**, *548* (7669), 567−572.

(42) Santos, A. L.; van Venrooy, A.; Reed, A. K.; Wyderka, A. M.; García-López, V.; Alemany, L. B.; Oliver, A.; Tegos, G. P.; Tour, J. M.

Hemithioindigo-based visible light-activated molecular machines kill bacteria by oxidative damage. *Adv. Sci.* **2022**, *9* (30), No. 2203242.

(43) Yang, H.; Yi, J.; Pang, S.; Ye, K.; Ye, Z.; Duan, Q.; Yan, Z.; Lian, C.; Yang, Y.; Zhu, L. A light-driven molecular machine controls K$^+$ channel transport and induces cancer cell apoptosis. *Angew. Chem., Int. Ed.* **2022**, *134* (26), No. e202204605.

(44) Chen, S.; Wang, Y.; Nie, T.; Bao, C.; Wang, C.; Xu, T.; Lin, Q.; Qu, D.-H.; Gong, X.; Yang, Y.; et al. An artificial molecular shuttle operates in lipid bilayers for ion transport. *J. Am. Chem. Soc.* **2018**, *140* (51), 17992−17998.

(45) Ye, R.; Ren, C.; Shen, J.; Li, N.; Chen, F.; Roy, A.; Zeng, H. Molecular ion fishers as highly active and exceptionally selective K+ transporters. *J. Am. Chem. Soc.* **2019**, *141* (25), 9788−9792.

(46) Li, N.; Chen, F.; Shen, J.; Zhang, H.; Wang, T.; Ye, R.; Li, T.; Loh, T. P.; Yang, Y. Y.; Zeng, H. Buckyball-based spherical display of crown ethers for de novo custom design of ion transport selectivity. *J. Am. Chem. Soc.* **2020**, *142* (50), 21082−21090.

(47) Ren, C.; Chen, F.; Ye, R.; Ong, Y. S.; Lu, H.; Lee, S. S.; Ying, J. Y.; Zeng, H. Molecular swings as highly active ion transporters. *Angew. Chem., Int. Ed.* **2019**, *58* (24), 8034−8038.

(48) Li, Y.-H.; Zheng, S.; Legrand, Y.-M.; Gilles, A.; Van der Lee, A.; Barboiu, M. Structure-driven selection of adaptive transmembrane Na$^+$ carriers or K$^+$ channels. *Angew. Chem., Int. Ed.* **2018**, *57* (33), 10520−10524.

(49) Krauss, D.; Eisenberg, B.; Gillespie, D. Selectivity sequences in a model calcium channel: role of electrostatic field strength. *Eur. Biophys. J.* **2011**, *40* (6), 775−782.

(50) Ren, C.; Ding, X.; Roy, A.; Shen, J.; Zhou, S.; Chen, F.; Yau Li, S. F.; Ren, H.; Yang, Y. Y.; Zeng, H. A halogen bond-mediated highly active artificial chloride channel with high anticancer activity. *Chem. Sci.* **2018**, *9* (17), 4044−4051.

(51) McNally, B. A.; O'Neil, E. J.; Nguyen, A.; Smith, B. D. Membrane Transporters for Anions That Use a Relay Mechanism. *J. Am. Chem. Soc.* **2008**, *130* (51), 17274−17275.

(52) Johnson, T. G.; Sadeghi-Kelishadi, A.; Langton, M. J. A photo-responsive transmembrane anion transporter relay. *J. Am. Chem. Soc.* **2022**, *144* (23), 10455−10461.

(53) Jo, S.; Lim, J. B.; Klauda, J. B.; Im, W. CHARMM-GUI membrane builder for mixed bilayers and its application to yeast membranes. *Biophys. J.* **2009**, *97* (1), 50−58.

(54) Essmann, U.; Perera, L.; Berkowitz, M. L.; Darden, T.; Lee, H.; Pedersen, L. G. A smooth particle mesh Ewald method. *J. Chem. Phys.* **1995**, *103* (19), 8577−8593.

(55) Jorgensen, W. L.; Chandrasekhar, J.; Madura, J. D.; Impey, R. W.; Klein, M. L. Comparison of simple potential functions for simulating liquid water. *J. Chem. Phys.* **1983**, *79* (2), 926−935.

(56) Xu, F.; Liu, C.; Zhou, D.; Zhang, L. TGF-β/SMAD pathway and its regulation in hepatic fibrosis. *J. Histochem. Cytochem.* **2016**, *64* (3), 157−167.